RbMn$_4$(AsO$_4$)$_3$: Molten-Salt Synthesis, Structure, and Magnetic Properties of a New Manganese(II) Arsenate

Richard MacKay,† Tina A. Wardojo,‡ and Shiou-Jyh Hwu†,[1]

†*Department of Chemistry, Clemson University, Clemson, South Carolina 29634; ‡Department of Chemistry, Rice University, P.O. Box 1892, Houston, Texas 77251*

Crystals of RbMn$_4$(AsO$_4$)$_3$ have been grown in an eutectic flux of CsCl/RbCl. The X-ray single-crystal structure analysis shows that the rubidium manganese(II) arsenate crystallizes in an orthorhombic lattice with $a = 10.109(1)$ Å, $b = 17.408(1)$ Å, $c = 6.552(1)$ Å, and $V = 1153.0(2)$ Å^3; *Pnnm* (No. 58); $Z = 4$. The structure is refined by the least-squares method to a final solution with R/R_w/GOF = 0.027/0.032/2.09. The compound is isostructural with KFe$_4$(PO$_4$)$_3$. The new structure description based on the heteropoly [As$_2$Mn$_3$O$_{16}$] structural units and the detailed account of extended framework formation based on Mn–O linkages are given. The Rb cations reside in the channels and coordinate with [6 + 2] oxygen atoms in an unusual geometry of bicapped trigonal prism where two capping O atoms are directed out beyond the opposite triangular faces of the prism. The observed Mn–O bond distances, BVS calculations, and magnetic susceptibility analysis suggest that the title compound contains high-spin, divalent (d^5) manganese cations. An antiferromagnetic transition is observed at ca. 7.5 K. Structure and bonding of RbMn$_4$(AsO$_4$)$_3$ vs KFe$_4$(PO$_4$)$_3$, with respect to the transition-metal-oxide framework, are discussed. Comparison to the structurally distinct phases of AMn$_4$(AsO$_4$)$_3$ (A = Na, K) is briefly presented. © 1996 Academic Press, Inc.

INTRODUCTION

A wealth of important information with regard to structure and bonding of inorganic solids becomes available from new materials made due to the effort in chemical synthesis via new approaches. The molten-salt methods have been proven effective in that the employed halide fluxes provide a convenient media for phase nucleation and crystallization of refractory ceramic materials (1). Using CsCl/A^{I}Cl eutectic fluxes, two new manganese(II) arsenates AMn$_4$(AsO$_4$)$_3$ (A = Na and K, respectively) were isolated (2). The framework contains edge-shared, pseudo-one-dimensional [MnO$_4$]$_\infty$ chains. An unusual chain made of distorted MnO$_6$ trigonal prisms is observed for the first time. The structural analysis shows that the unique trigonal prismatic coordination geometry around Mn results from the Mn-site disordering. Correlation studies based on the crystal field theory and magnetic susceptibility reveal that the disordered structure is stabilized by the preferred energy state for the high-spin d^5 electron configuration.

Employing the CsCl/RbCl eutectic flux, the title compound was isolated. Unlike the Na and K analogs, the RbMn$_4$(AsO$_4$)$_3$ framework consists of layers separated by a distinct tunnel structure around the Rb cations. The effect to the extended lattice because of different size (3) as well as concentration (4) of electropositive cations has been previously demonstrated by some titanium phosphate compounds, e.g., ATiP$_2$O$_7$ (A = K, Rb, Cs) and the NASICON-related Li$_{1+x}$Ti$_2$(PO$_4$)$_3$ ($0 \leq x \leq 2$) series, respectively. In this report we present a detailed account of the Mn–O framework in RbMn$_4$(AsO$_4$)$_3$, which was not described in the discussion of the otherwise isostructural compound KFe$_4$(PO$_4$)$_3$ (5). Structural comparison to the AMn$_4$(AsO$_4$)$_3$ (A = Na, K) analogs is briefly discussed.

EXPERIMENTAL

Synthesis. Single crystals of RbMn$_4$(AsO$_4$)$_3$ were synthesized using As$_2$O$_5$ (0.53 mmole) (Aesar, 99.99%) and MnO (1.06 mmole) (Aesar, 99.5%) to prepare a reaction mixture (charge) with nominal composition Mn$_2$As$_2$O$_7$. The eutectic flux used was 40% CsCl (Aldrich, 99%) and 60% RbCl (Strem, 99.9%) by moles; mp = 646°C. The flux to charge ratio was approximately 5.1:1 by weight. The resulting mixture was loaded in a nitrogen-purged dry box into a carbon-coated, quartz ampoule which was then sealed under vacuum. The ampoule was heated at a slow rate (20 ~ 25°C/h) to 300°C and maintained at that temperature for 4 days, followed by heating at 800°C for 4 days. The final steps involved slow cooling at 3°C/h to 600°C, followed by cooling at 40°C/h to room temperature. The crystalline phases were retrieved from the flux by washing the products with deionized water using a suction filtration method. Clear, colorless crystals in a small, flat needle-

TABLE 1
Crystallographic Data for RbMn₄(AsO₄)₃

Formula weight (g/mol)	721.98
Space group	*Pnnm* (#58)
a(Å)	10.109(1)
b(Å)	17.408(1)
c(Å)	6.552(1)
V(Å³)	1153.0(2)
Z	4
Temperature	150 K
ρ_{calc} (g/cm³)	4.16
Radiation (graphite monochromated)	Mo$K\alpha$
Crystal shape, color, size (mm)	needle, colorless, $0.03 \times 0.06 \times 0.22$
Linear absorption coefficient (cm⁻¹)	170.72
Transmission factors	0.70–1.00
Scan type/Scan range (deg.)	$2\theta - \omega / -0.735 + 0.350 \tan \theta$
Scan speed (deg/min)	8, with up to 3 rescans
2θ range	3.6–60.0
Indices	$0 \rightarrow h, 0 \rightarrow k, -l \rightarrow l$
No. of reflections measured	3854
No. of unique reflections (R_{int})	1973 (0.03)
No. of unique reflections with $I > 3\sigma(I)$	1409
No. of variables	110
F_{000}	1212
p for $\sigma(F^2)$	0.005
$R(F)^a/R_w(F)^b$/GOF	0.027/0.032/2.09

[a] $R = \Sigma[|F_o| - |F_c|]/\Sigma|F_o|$.
[b] $R_w = [\Sigma w[|F_o| - |F_c|]^2/\Sigma w|F_o|^2]^{1/2}$.

shaped morphology were isolated. An unidentified phase was also present as small dark flakes. The yield of the reaction products was undetermined since the reaction vessel shattered during the synthesis.

Structure determination. Colorless crystals of Rb Mn₄(AsO₄)₃ were mounted on glass fibers for single crystal X-ray diffraction study. The diffraction data were collected under a cold flow of nitrogen ($T = 150$ K) on a Rigaku AFC7R four-circle diffractometer. Crystallographic data for the title compound are summarized in Table 1. The unit cell parameters and the orientation matrix were determined by a least-squares fit of 25 randomly located reflections with $10° < 2\theta < 14°$. Data were collected using an $\omega - 2\theta$ scan mode at 8°/min (≤3 rescans). A total of 3854 reflections ($2\theta_{max} = 60°$) were collected on the primitive orthorhombic cell from two octants ($h, k, \pm l$), of which 1973 reflections with $I > 3\sigma(I)$ were used for the structure solution. There was no detectable decay during the data collection, according to the intensities of three standard reflections which were measured every 100 reflections. Lorentz-polarization and empirical absorption corrections (psi scans) were applied to the data (6). On the basis of extinction conditions and successful structure solution,

space group *Pnnm* (No. 58) was chosen. The structure was solved by direct methods with SHELXS-86 (7), and refined on $|F|$ with teXsan (8) by least-squares, full-matrix techniques (9). Scattering factors for all atoms were taken from the source program used. Figures were drawn with SHELXS-Plus (10). Table 2 lists the positional and thermal parameters. For ease of comparison with the KFe₄(PO₄)₃ structure, which was reported in a nonstandard setting (*Pmnn*), the numbering of atoms was kept the same after transformation to the standard setting. Table 3 gives selected bond distances and angles.

Magnetic measurement. The magnetic susceptibility was measured using a Quantum Design SQUID MPMS-5S magnetometer at field strength 0.5 T in the temperature range 1.74–300 K. Selected single crystals (5.6 mg) were contained in a gel capsule sample holder which was suspended in a straw from the sample translator drive. The temperature and field dependence of the susceptibility of the container were previously determined and their effect was negligible. The magnetic susceptibility was corrected for core diamagnetism with Pascal's constants (11).

RESULTS AND DISCUSSION

Structure description. Although the role of molten salt in phase nucleation has not been fully studied, the formation of the title compound appeared to occur as a result of cation inclusion from the eutectic flux. Prior syntheses of the AMn₄(AsO₄)₃ (A = Na, K) phases have revealed a trend that appears to govern the incorporation of electropositive cations (A). In agreement with other cases studied

TABLE 2
Positional and Thermal Parameters[a] for RbMn₄(AsO₄)₃

Atom	x	y	z	B_{eq}(Å²)
Rb	0.30777(7)	0.46568(4)	0	0.92(3)
As(1)	0.04569(7)	0.33441(4)	0	0.48(3)
As(2)	0.45619(7)	0.27685(4)	0	0.50(3)
As(3)	0.20663(7)	0.03716(4)	0	0.59(3)
Mn(1)	0.5407(1)	0.09184(6)	0	0.56(4)
Mn(2)	0.9752(1)	0.14520(6)	0	0.59(4)
Mn(3)	0.24788(7)	0.20109(4)	0.2532(1)	0.64(2)
O(1)	0.1210(5)	0.6777(3)	0	0.8(2)
O(2)	0.6236(5)	0.2708(3)	0	0.7(2)
O(3)	0.0963(3)	0.3805(2)	0.2073(6)	0.8(1)
O(4)	0.3889(5)	0.1859(3)	0	0.7(2)
O(5)	0.1156(5)	0.2438(3)	0	0.7(2)
O(6)	0.8643(5)	0.0486(3)	0	1.2(2)
O(7)	0.1563(3)	0.0914(2)	0.1993(6)	1.0(1)
O(8)	0.3937(3)	0.3157(2)	0.2132(6)	0.9(1)
O(9)	0.3702(5)	0.0207(3)	0	1.0(2)

[a] Equivalent isotropic thermal parameter defined as $B_{eq} = (8\pi^2/3)$ trace U.

TABLE 3
Selected Interatomic Distances (Å) and
Angles (deg) in RbMn$_4$(AsO$_4$)$_3$

[MnO$_5$] trigonal bipyramid			
Mn(1)–O(3)	2.055(4) × 2	Mn(1)–O(9)′	2.156(5)
Mn(1)–O(9)	2.122(5)	Mn(1)–O(4)	2.244(5)
O(3)–Mn(1)–O(3)	137.8(2)	O(4)–Mn(1)–O(9)	82.6(2)
O(3)–Mn(1)–O(4)	90.9(1) × 2	O(4)–Mn(1)–O(9)′	161.6(2)
O(3)–Mn(1)–O(9)	111.0(1)	O(9)–Mn(1)–O(9)′	79.0(2)
O(3)–Mn(1)–O(9)′	95.6(1) × 2		
[MnO$_6$] octahedra			
Mn(2)–O(6)	2.022(5)	Mn(2)–O(5)	2.228(5)
Mn(2)–O(8)	2.162(4) × 2	Mn(2)–O(7)	2.437(4) × 2
O(5)–Mn(2)–O(6)	174.1(2)	O(7)–Mn(2)–O(7)	64.8(2)
O(5)–Mn(2)–O(7)	79.5(1) × 2	O(7)–Mn(2)–O(8)	150.8(1) × 2
O(5)–Mn(2)–O(8)	90.0(1) × 2	O(7)–Mn(2)–O(8)	86.7(1) × 2
O(6)–Mn(2)–O(7)	95.6(1) × 2	O(8)–Mn(2)–O(8)	120.7(2)
O(6)–Mn(2)–O(8)	92.9(1) × 2		
Mn(3)–O(2)	2.105(3)	Mn(3)–O(4)	2.204(3)
Mn(3)–O(1)	2.130(3)	Mn(3)–O(5)	2.257(3)
Mn(3)–O(7)	2.151(3)	Mn(3)–O(8)	2.494(3)
O(1)–Mn(3)–O(2)	80.4(1)	O(2)–Mn(3)–O(8)	104.3(2)
O(1)–Mn(3)–O(4)	98.4(1)	O(4)–Mu(3)–O(5)	82.5(1)
O(1)–Mn(3)–O(5)	171.8(2)	O(4)–Mn(3)–O(7)	92.8(2)
O(1)–Mn(3)–O(7)	102.9(2)	O(4)–Mn(3)–O(8)	68.5(1)
O(1)–Mn(3)–O(8)	82.2(1)	O(5)–Mn(3)–O(7)	85.2(2)
O(2)–Mn(3)–O(4)	172.9(2)	O(5)–Mn(3)–O(8)	90.5(2)
O(2)–Mn(3)–O(5)	97.7(1)	O(7)–Mn(3)–O(8)	161.2(1)
O(2)–Mn(3)–O(7)	94.4(2)		
[AsO$_4$] tetrahedra			
As(1)–O(3)	1.659(4) × 2	As(1)–O(5)	1.728(5)
As(1)–O(1)	1.698(5)		
O(1)–As(1)–O(3)	111.5(1) × 2	O(3)–As(1)–O(3)	109.9(2) × 2
O(1)–As(1)–O(5)	107.0(2)	O(3)–As(1)–O(5)	108.4(1)
As(2)–O(8)	1.676(4) × 2	As(2)–O(4)	1.723(4)
As(2)–O(2)	1.695(5)		
O(2)–As(2)–O(4)	109.7(2)	O(4)–As(2)–O(8)	102.8(1) × 2
O(2)–As(2)–O(8)	113.7(1) × 2	O(8)–As(2)–O(8)	113.0(2)
As(3)–O(6)	1.655(5)	As(3)–O(7)	1.690(4) × 2
As(3)–O(9)	1.679(5)		
O(6)–As(3)–O(7)	111.9(2) × 2	O(7)–As(3)–O(7)	101.2(3)
O(6)–As(3)–O(9)	105.8(2)	O(7)–As(3)–O(9)	113.1(2) × 2
[RbO$_6$] polyhedron			
Rb–O(3)	2.935(4) × 2	Rb–O(8)	3.087(4) × 2
Rb–O(7)	2.967(4) × 2	Rb–O(6)	3.335(1) × 2

(2a), the smaller cation *A*, either mono- or divalent, becomes incorporated into the arsenate product from the eutectic halide flux CsCl/ACl. Note that KFe$_4$(PO$_4$)$_3$ was also isolated from a cation-incorporation reaction in the KCl-added Fe$_2$O$_3$–(NH$_4$)$_2$HPO$_4$–H$_2$O system (5).

The title compound is isostructural with KFe$_4$(PO$_4$)$_3$ adopting a channel structure running along *a*. The extended structure is made of parallel slabs of mixed Mn–O/As–O networks that are connected through additional Mn–O trigonal bipyramids and As–O tetrahedra to form

channels where the Rb atoms reside. The slab has a wave-like appearance (Fig. 1) with an approximate thickness of 5.92 Å. The cross section of channels on the *bc* plane is 5.57 Å along *b* and 6.55 Å along *c* directions, which are dispersed around 5.94 Å, the 2 × (Rb–O) distance according to Shannon (12). The nearest Rb–O contacts around each Rb atom form an unusual [6 + 2] bicapped trigonal prismatic coordination where two capping O atoms are directed out beyond the opposite triangular faces of the prism. The six Rb–O distances of the prism are 2.93–3.09 Å while the two long Rb–O are 3.34 Å.

The Mn–O framework will be the primary focus of this study; the comparison with the corresponding Fe–O network, which was not discussed in the structure of KFe$_4$(PO$_4$)$_3$, and the framework versatility will be addressed. A section of the Mn–O network (Fig. 1) of the mixed (Mn–O/As–O) slab is projected onto the *ab* plane along with the additional Mn(1)–O polyhedra that connect the slabs. This extended Mn–O framework is composed of distorted, Mn(1)-centered oxygen trigonal bipyramids and Mn(2)- and Mn(3)-centered octahedra. The Mn(2)- and Mn(3)-centered octahedra condense to form a buckled layer along the *ac* plane. The layer is comprised of 1D chains of edge-shared Mn(3)O$_6$ octahedra perpendicular to the *ab* plane joined together by corner- and edge-shared Mn(2)O$_6$ octahedra. The trigonal bipyramidal (tbp) Mn(1)O$_5$ shares its O(9)–O(9)′ edge (2.72 Å) across an inversion center to form a double tbp unit. These edge-shared tbp units link the Mn(2)/Mn(3) layers via corner-shared oxygen atoms, O(4), to extend the Mn–O framework along *b*.

A detailed view of the Mn(2)- and Mn(3)-centered octahedral layer is shown in Fig. 2. The two parallel, edge-shared [Mn(3)O$_4$]$_\infty$ chains are oriented approximately orthogonal to each other with respect to their square planes but are not in direct contact (Fig. 2a). The Mn(3)–Mn(3) bond distance across the shared edge alternates in long and short distances, 3.319 (2) Å for Mn(3a)–Mn(3b) and 3.234 (2) Å for Mn(3b)–Mn(3c). A similar feature has been seen with respect to the rutile chain in the La$_4$Ti(Si$_2$O$_7$)$_2$(TiO$_2$)$_{4m}$ series (1a). The polyhedral illustration in Fig. 2b shows that Mn(2) lies in the long separation gap between chains and shares two edges with adjacent Mn(3) octahedra. Two of the vertices of the Mn(2)O$_6$ octahedra, O(8), are shared with two apical oxygens on an adjacent Mn(3) chain to form an extended lattice along *a*.

Alternatively, the Mn–O slab can be viewed as formed by heteropoly [As$_2$Mn$_3$O$_{16}$] units, as shown in Fig. 3. The unit is composed of a 3-octahedral subunit and 2 edge-shared [AsO$_4$] tetrahedra, a building block similar to that seen, for example, in Keggin structures (13). The "trimeric" subunits are fused together through the opposite edges along the Mn(3)–Mn(3) octahedral chain as well as
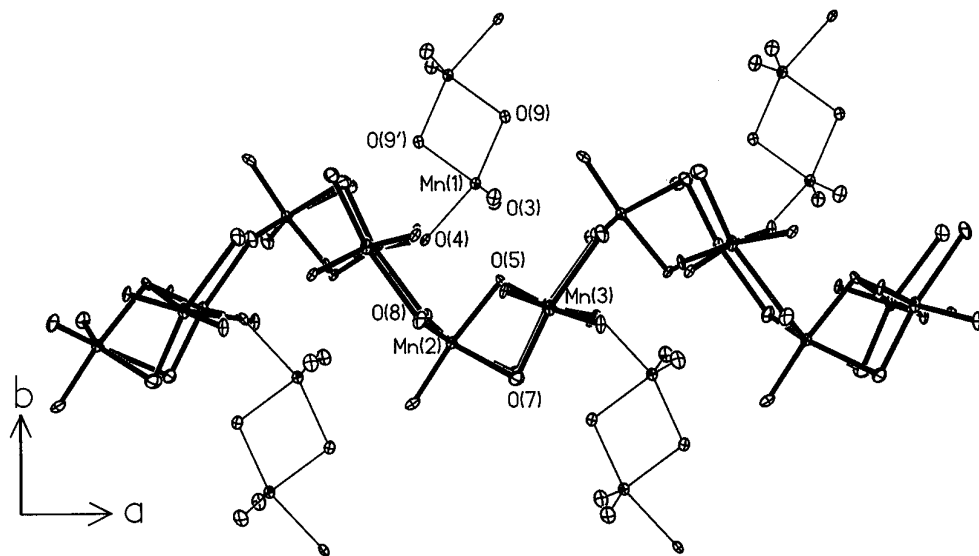
FIG. 1. Mn–O network within the slab. Mn(2) and Mn(3) centered octahedra form buckled layers (thick lines). Edge-shared trigonal bipyramids around Mn(1) (thin lines) link adjacent layers. The anisotropic thermal ellipsoids are drawn in 70% probability.

through the corners of Mn(2)–Mn(3) octahedra between chains to form the slab.

The Mn–O distances (Table 3) along with the bond valence sum (BVS) evaluations suggest that the title compound contains high-spin (HS), divalent (d^5) manganese cations. The Mn(1)–O distances range from 2.06 to 2.24 Å. The average distance is 2.13 Å, comparable with the sum of Shannon crystal radii (12), 2.10 Å, of five-coordinated Mn^{2+} (0.89 Å, HS) and O^{2-} (1.21 Å). Mn(2) is surrounded by four oxygens from 2.02 to 2.23 Å, plus

two at 2.44 Å. This [4 + 2] coordination gives a distorted octahedral geometry, similarly observed in the iron phosphate. The Mn(3) atom is surrounded by five oxygens at 2.11–2.26 Å, with an additional oxygen at 2.49 Å. In the iron phosphate the Fe–O distances range from 2.07 to 2.19 Å, with the sixth oxygen at a much longer distance 2.51 Å. Consequently, the latter was described as square pyramidal in the $KFe_4(PO_4)_3$ structure. In any case, the average Mn–O distances are 2.24 and 2.22 Å, respectively, comparable with 2.14–2.24 Å observed in the (Na, K)
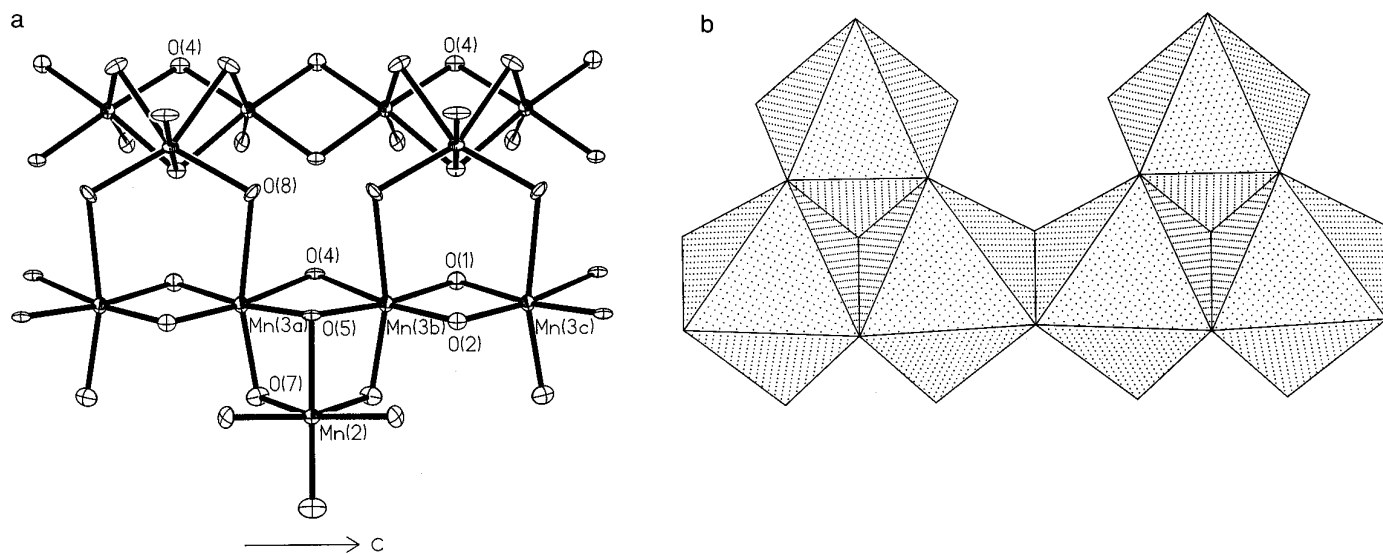

FIG. 2. (a) Edge-shared chains of Mn(3)-centered octahedra joined by Mn(2). Shared octahedral edges have lengths 2.733(7) Å (O(1)–O(2)), 2.941(7) Å (O(4)–O(5)), and 2.985(5) Å (O(5)–O(7)). (b) Polyhedral drawing of the edge-shared octahedral chain, see text.
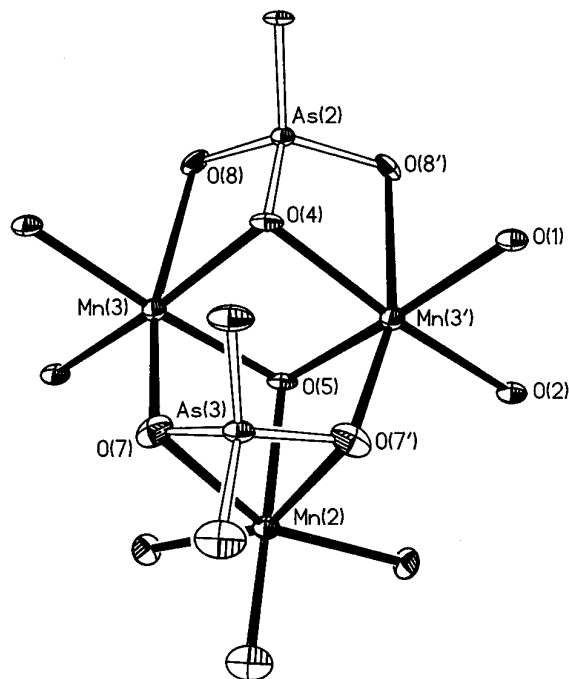
FIG. 3. The heteropoly [As$_2$Mn$_3$O$_{16}$] unit. Angles around bridging oxygens are 94.0(1)°, 94.6(2)°, 97.1(2)°, and 97.7(2)° for Mn(2)–O(7)–Mn(3), Mn(3)–O(5)–Mn(3), Mn(2)–O(5)–Mn(3), and Mn(3)–O(4)–Mn(3), respectively. The anisotropic thermal ellipsoids are drawn in 70% probability.

the above mentioned square-planar [FeO$_5$] unit. Furthermore, the formation of the nearly 90° Mn–O–Mn angles, 94.0 (1)°–97.7 (2)°, is attributed to the edge-sharing configuration. These angles are less than 98°, an upper-limit angle for the possible ferromagnetic coupling in oxobridged magnetic centers (15). It should be noted that, however, most of the bridging angles in the Mn–O framework are larger than 98° which is consistent with the weak antiferromagnetic coupling measured (see below).

Structurally, the new RbMn$_4$(AsO$_4$)$_3$ is distinct compared to the recently discovered AMn$_4$(AsO$_4$)$_3$ (A = Na, K) phases. Due to the structure versatility, many compound series adopt similar structural units and change only their packing arrangement to accommodate different size alkali metal cations, as illustrated by the ATiP$_2$O$_7$ (A = K, Rb, Cs) family (3). In this case, not only is the coordination around the alkali metal cations different, but the metal oxide frameworks are unrelated. Figure 4 shows the Rb-centered channel structure where the Rb cations are coordinated with [6 + 2] oxygen atoms in the above mentioned unusual geometry of a bicapped trigonal prism. This is quite different than the (Na, K)Mn$_4$(AsO$_4$)$_3$ structure where the electropositive cations reside in the channels made of alternating edges of three MnO$_6$ octahedra and three AsO$_4$ tetrahedra.

Magnetic properties. As portrayed in Fig. 5, the plot of χ_m^{-1} (inverse molar susceptibility) versus T (temperature)
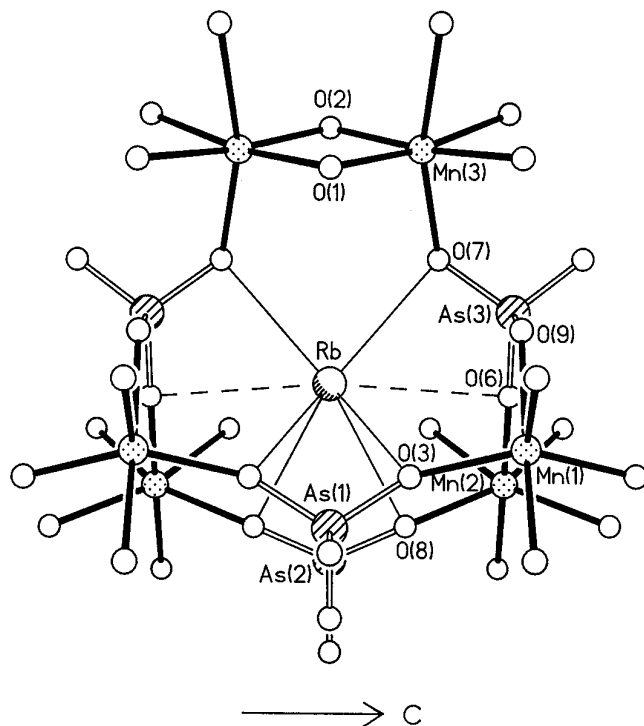
Mn$_4$(AsO$_4$)$_3$ analogs (2) containing a high-spin d^5 Mn^{2+} cation. The former distances are slightly longer than 2.18 Å, the sum of Shannon crystal radii of six-coordinated Mn^{2+} (0.97 Å, HS) and O^{2-}, but much longer than 2.03 Å, the predicted Mn–O distance for the low-spin Mn^{2+} cation. The divalent oxidation state is supported by the BVS calculations (14) for Mn(1), Mn(2), and Mn(3) giving the values 2.05, 1.93, and 1.96, respectively.

The tetrahedra around As(1), As(2), and As(3) are all slightly distorted (Table 3). The range of As–O distances is narrower than that of the corresponding P–O distances in KFe$_4$(PO$_4$)$_3$. However, the O–As–O angles deviate more from the ideal tetrahedral angle and from the corresponding [PO$_4$] units. The small angles, 101.2(3)° for O(7)–As(3)–O(7c) and 102.8(1)° for O(4)–As(2)–O(8), are associated with the shared O–O edges between an As-centered tetrahedron and a Mn-centered octahedron. As(2) shares two adjacent edges with two Mn(3) octahedra while As(3) shares an edge with a Mn(2)-centered octahedron (Fig. 3). The smaller angle reduces cation–cation repulsion without significant lengthening in As–O bond or change in bond strength. Because of the short P–O bond, this distortion is not as easily accommodated in phosphates, particularly that corresponding to the double-edge-shared As(2)O$_4$. It therefore results in a long Fe–O bond and, consequently,

FIG. 4. Rb-centered channel structure.

FIG. 5. Susceptibility data for RbMn₄(AsO₄)₃, plotted as χ_m^{-1} versus T.

shows that $RbMn_4(AsO_4)_3$ obeys the ideal Curie–Weiss type parmagnetic behavior over the range ca. 20–300 K and undergoes an antiferromagnetic ordering at ~7.5 K (see inset). The paramagnetic data were fitted to the Curie–Weiss equation, $\chi = \chi_o + C/(T - \theta)$, where χ_o is the temperature-independent paramagnetism, C is the Curie constant, and θ is the Weiss constant. The model yielded best-fit values of $\chi_o = -0.050$ emu/mole, $C = 3.92$ emu-K/mole, and $\theta = -44.70$ K, corresponding to a μ_{eff} of 5.62 μ_B, which is slightly lower than the ideal value of 5.92 μ_B for a single manganese(II), high-spin d^5. The negative χ_o and low μ_{eff} probably resulted from unaccounted diamagnetic contribution from quartz impurities mixed in with the sample, since the appearance of the crystals was very similar to that of quartz fibers. Otherwise, the data show a nearly perfect fit with the Curie–Weiss law. The antiferromagnetic transition is consistent with the negative Weiss constant θ. The low onset temperature of the transition is attributed to the weak magnetic coupling via the Mn–O–Mn superexchange.

Despite the complexity of the theoretical prediction concerning the magnetic coupling of $RbMn_4(AsO_4)_3$, a high-spin d^5 system, the superexchange via Mn–O–Mn can perhaps be described in terms of the overlap of the d orbitals on the Mn^{2+} cation with s and p orbitals on the O^{2-} anion (16). The $p\sigma$ and $p\pi$ orbitals of the anion can both be

involved in the superexchange interactions (16b). Although the sign of the superexchange interaction (which determines whether the ordering is ferro- or antiferromagnetic) arising from the sum of each orbital overlap is uncertain, the ensuing superexchange interaction in this case is nevertheless antiferromagnetic.

REFERENCES

1. See examples and references cited therein: (a) S. Wang, S.-J. Hwu, J. A. Paradis, and M.-H. Whangbo, *J. Am. Chem. Soc.* **117,** 5515 (1995); (b) J. D. Carpenter and S.-J. Hwu, *Inorg. Chem.* **34,** 4647 (1995).
2. (a) T. A. Wardojo, MA Thesis, Rice University (1995); (b) T. A. Wardojo, R. Mackay, S.-J. Hwu, and W. T. Pennington, to be submitted, 1996.
3. S. Wang and S.-J. Hwu, *J. Solid State Chem.* **92,** 219 (1991).
4. S. Wang and S.-J. Hwu, *Chem. Mater.* **4,** 589 (1992).
5. E. N. Matvienko, O. V. Yakubovich, M. A. Simonov, and N. V. Belov, *Dokl. Akad. Nauk SSSR* **259,** 591 (1981); *Sov. Phys. Dokl.* **26,** 633 (1981).
6. A. C. T. North, D. C. Phillips, and S. F. Mathews, *Acta Crystallogr.* **351,** 351 (1968).
7. G. M. Sheldrick, *in* "Crystallographic Computing 3" (G. M. Sheldrick, C. Krüger, and R. Goddard, Eds.), pp. 175–189. Oxford Univ. Press, London/New York, 1985.
8. (a) "teXsan: Single Crystal Structure Analysis Software, Version 1.6b." Molecular Structure Corp., The Woodlands, TX, 1993; (b) D. T. Cromer and J. T. Waber, *in* "International Table for X-ray Crystallography," Vol. IV, Table 2.2A, pp. 71–98. Kyroch Press, Birmingham, UK, 1974.
9. W. R. Busing, K. O. Martin, and H. A. Levy, "*ORFLS*," Report ORNL-TM-305, Oak Ridge National Laboratory, Oak Ridge, TN, 1962.
10. G. M. Sheldrick, "SHELXTL-Plus, Version 4.2.1. Structure Determination Software Programs," Siemens Analytical X-ray Instruments Inc., Madison, Wisconsin, 1990.
11. C. J. O'Connor, *Prog. Inorg. Chem.* **29,** 203 (1982).
12. R. D. Shannon, *Acta Crystallogr. A* **32,** 751 (1976).
13. A. F. Wells, "Structural Inorganic Chemistry," 5th ed., p. 521. Oxford Univ. Press, New York, 1984.
14. N. Brese and M. O'Keefe, *Acta Crystallogr. B* **47,** 192 (1991).
15. P. J. Hay, J. C. Thilbeault, R. Hoffmann, *J. Am. Chem. Soc.* **97,** 4884 (1975).
16. (a) D. J. Hodgson, *Prog. Inorg. Chem.* **19,** 173 (1975); (b) J. Kanamori, *Phys. Chem. Solids* **10,** 87 (1959).